AIAA JOURNAL
Vol. 52, No. 1, January 2014

Technical Notes

Effects of Corrugated Aerofoil Surface Features on Flow-Separation Control

T. H. New,* Y. X. Chan,† and G. C. Koh†
Nanyang Technological University, Singapore 639798, Republic of Singapore
M. C. Hoang‡
National University of Singapore, Singapore 129957, Republic of Singapore
and
Shengxian Shi§
Shanghai Jiao Tong University, Shanghai 200240, People's Republic of China

DOI: 10.2514/1.J052398

I. Introduction

WITH increased awareness of the potential engineering benefits in emulating certain aspects of insect wings or insect flight mechanics, it is not surprising that there is recent surge of interest in their investigations for lift generation or stall mitigation. Other than exploring how the exact flapping/heaving mechanisms employed by insects contribute toward their agility during flight [1–8], understanding how unique surface geometries and features of insect wings enable these insects to maneuver the way they do is also one of the major research motivations for some recent studies. Of interest to the present study are investigations conducted by Hu and Tamai [9], Murphy and Hu [10], and Levy and Seifert [11] recently, where they looked at the flow dynamics of aerofoils based on dragonfly wing cross sections. Hu and Tamai [9] and Murphy and Hu [10] studied corrugated aerofoils with cross sections resembling typical dragonfly wing cross sections and observed favorable aerodynamic behavior. They noted that flow-separation vortices trapped within the corrugation valleys draw fluid toward the aerofoil wall region and reduce the overall extent of the flow-separation region. These unique flow features mean that flow separations can be delayed until a higher angle of attack with accompanying increases in lift-to-drag ratios for these corrugated aerofoils up to a chord Reynolds number of $Re = 125,000$.

On the other hand, the corrugated aerofoil studied by Levy and Seifert [11] had far fewer corrugations. Instead, their aerofoil had only two corrugations close to the leading edge, followed by a "saddle" and convex trailing-edge "hump". Because of this geometric difference, the mechanisms with which this aerofoil is able to delay flow separation are different. In this case, flow separations arising from the upstream corrugations reattach back to the trailing-edge hump regularly, which translates into fewer flow-separation events propagating beyond the trailing edge. In particular, a recirculating vortex is observed to form at the saddle, which is believed to play an important role in controlling flow separation. It should be mentioned that Hu and Tamai [9] performed their experiments at $Re = 34,000$, and Murphy and Hu [10] conducted theirs at $Re = 58,000$ to 125,000, whereas Levy and Seifert [11] performed their investigations at $Re < 8000$. In addition, the ranges of angle of attack investigated between these studies were also different.

It is clear from the earlier studies that the vortex formation and behavior along the upper surfaces of corrugated aerofoils drive the favorable flow effects seen so far. Although some insights into their behavior have been provided by the earlier studies, direct comparisons between them were difficult due to the different test conditions used. To do that, they have to be studied under similar flow conditions, and this provided the primary motivation for the present study. To accomplish that, an experimental flow visualization and particle image velocimetry (PIV) investigation was performed in this study to compare the differences in the near-field vortical behavior and the extent to which flow separation is mitigated between these two corrugated aerofoils at a fixed chord Reynolds number of $Re = 14,000$. The use of a relatively low Reynolds number here will not only provide additional insights into the basic aerodynamic characteristics of dragonfly wings but also shed light on the use of different corrugated aerofoils in micro aerial vehicles as well.

II. Experimental Setup

The experiments were conducted in a low-speed recirculating water tunnel with a test section measuring 450 (W) × 600 (H) × 1500 mm (L). The test section was constructed from glass, which allowed good optical access from the sides and bottom. Water was recirculated throughout the water tunnel by an axial pump, and it was conditioned using honeycombs, fine screens, and a contraction section before entering the test section. The experimental setup used here is shown in Fig. 1, where two flat end plates were located at both ends of the 300-mm-long, 75-mm-chord test aerofoils. A stepper motor was used to vary the aerofoil angle of attack and was attached to the aerofoils via a coupling at their quarter-chord locations. The Reynolds number used during the experiments was approximately $Re = Uc/\nu = 14,000$, where U is the mean freestream velocity, c is the aerofoil chord length, and ν is water kinematic viscosity at working conditions. Freestream turbulence intensity was estimated to be 1.1% at the working freestream velocity of $U = 0.19$ m/s, as determined from time- averaged PIV measurements taken at the region where the aerofoils were to be mounted. Last, uncertainty in the freestream Reynolds number has also been ascertained to be approximately ±1.2%.

Two different corrugated aerofoils were studied; the first one was based on a typical dragonfly wing cross section investigated by Hu and Tamai [9] and Murphy and Hu [10], while the second one was based on a simplified dragonfly wing cross section studied by Levy and Seifert [11]. To ease identification of the aerofoils here, they will be known as corrugated A and B, respectively. As indicated in Fig. 2, the design of corrugated A aerofoil consisted of a series of nonuniform sharp peaks and valleys. On the other hand, corrugated B aerofoil had two identical sharp peaks with a valley in between, followed by a rather significant but smooth hump. Geometries of the present corrugated aerofoils were designed according to the design rules provided in the aforementioned studies, and therefore their detailed design rules will not be elaborated. The leading-edge and trailing-edge thicknesses of corrugated A aerofoil were 3 mm, while those of corrugated B were 2 mm. For the sake of comparison, a

Received 18 October 2012; revision received 5 April 2013; accepted for publication 20 April 2013; published online 24 December 2013.

*Assistant Professor, School of Mechanical and Aerospace Engineering.
†Undergraduate Student, School of Mechanical and Aerospace Engineering.
‡Student, High School of Maths and Science.
§Lecturer, Key Laboratory for Power Machinery and Engineering of Ministry of Education, School of Mechanical Engineering.

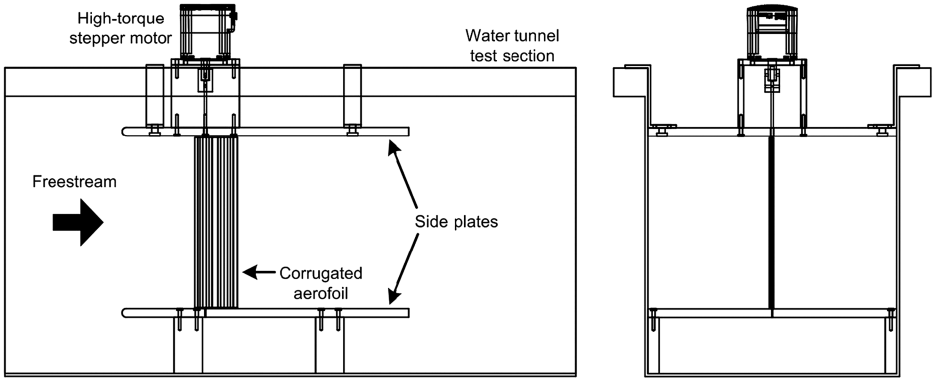

a) Side view b) End view

Fig. 1 Experimental apparatus and setup used in the present study.

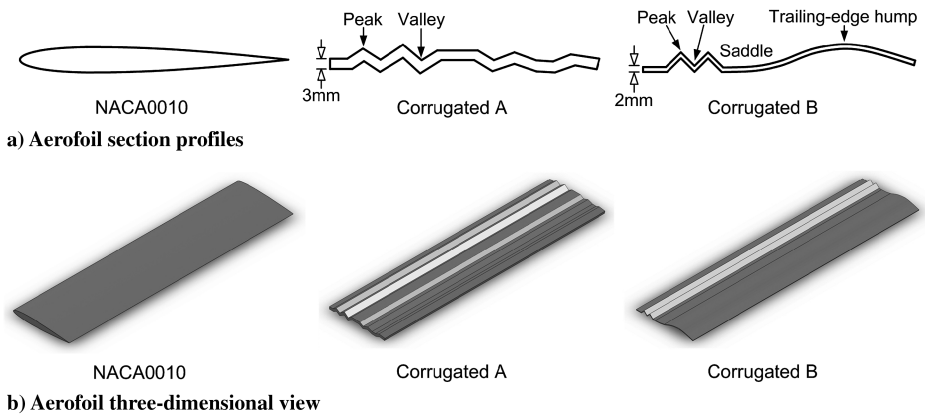

a) Aerofoil section profiles

b) Aerofoil three-dimensional view

Fig. 2 Cross-section profiles and three-dimensional views of the reference NACA 0010 and two corrugated aerofoils.

symmetrical NACA 0010 aerofoil was tested alongside with the corrugated aerofoils. It was selected because the maximum thickness-to-chord ratios for both corrugated aerofoils were approximately 10%, comparable to that of the NACA 0010 aerofoil. All aerofoil test models had spans and chords of $b = 300$ mm and $c = 75$ mm, respectively, which yielded a consistent aspect ratio of $b/c = 4$ throughout the study. This aspect ratio is higher than that in [9,10], where aerofoils of aspect ratio of $b/c \approx 3$ were investigated, as well as [11], where an aerofoil of relatively low aspect ratio of $b/c \approx 2$ was studied.

Because higher-aspect-ratio aerofoils are much less likely to result in three-dimensional effects arising from the end walls and mounting mechanisms (i.e., at one of the end walls, in this case) than lower-aspect-ratio aerofoils, the flow behavior observed along the midspan of the test aerofoils here will be representative.

Note that, unlike the NACA 0010 aerofoil, both corrugated A and B aerofoils had different nonzero cambers. However, it is worthwhile to point out that the overall cambers of the two corrugated aerofoils were dissimilar to begin with, thus posing significant technical challenges and complexities when attempting to compare based on the notion of equivalent camber. On the other hand, making use of a similar maximum thickness-to-chord ratio was found to be more appropriate instead because it is still one of the most important geometrical characteristics of an aerofoil that affects flow-separation behavior. Last, all test aerofoils were fabricated from stainless steel blocks using wire-cutting techniques, with their surfaces smoothed down using sandpaper and spray painted matte black for the experiments.

Particle-streak visualizations were used to give a first-hand appreciation of the flowfields produced by the three aerofoils. In this case, 20 μm polyamide seeding particles were uniformly distributed within the water tunnel and a digital single-lens reflex camera with an $f1.8$, 50 mm manual lens located beneath the transparent water tunnel floor was used to capture the flowfields. To provide illumination, a 1 W LaVision 532 nm continuous-wave laser was used in conjunction with beam-steering and sheet-forming optics, such that the laser sheet was aligned along the midspan of the test aerofoils. The laser sheet was approximately 1.5 mm thick. Global velocity measurements of the flowfields were conducted using a two-dimensional PIV system. It was composed of a 200 mJ double-pulse Nd:YAG laser with sheet-forming optics, a 1600×1200 pixel double-frame charge-coupled-device camera with an $f2.8$, 28 mm lens attached, with synchronizing and image-grabbing cards housed in a workstation. The measurement plane was similar to the flow visualization plane used earlier. Twenty-micrometer polyamid seeding particles were premixed into the water-tunnel and double-frame, and single-exposure images of scattered light from the particles were captured by the system at 15 Hz. A total of 1000 image pairs (i.e., instantaneous velocity fields) were captured for each aerofoil at every angle of attack used to ensure satisfactory convergence in the mean flowfield characteristics.

The physical PIV measurement window was approximately 126.9×95.3 mm and was maintained throughout the study. All double-frame images were processed using multigrid cross correlation with initial and final interrogation window sizes of 128 and 32 pixels squared (i.e., approximately 10.2 and 2.5 mm^2, respectively) and 50% window overlapping in both directions. Based on the PIV measurement procedures, the velocity vector map resolution was approximately 1.25 mm/vector. Because the PIV experiments were performed according to the procedures recommended by Keane and Adrian [12], the uncertainty levels of the measured velocity components were limited to within $\pm 1\%$. Last, proper orthogonal decomposition (POD) analysis was performed on the PIV velocity fields to reconstruct the vorticity fields based on the first 50 modes, which took into account 86% of the flow energy. This was performed to better differentiate the dominant flow structures from the incoherent turbulent flow structures, such that effects of the aerofoil surface geometries on the overall flow-separation behavior can be

properly isolated. The methodology used in the POD analysis here followed those described by Sirovich [13], Berkooz et al. [14], and Chatterjee [15], where sequential vorticity fields were decomposed into corresponding sets of POD coefficients and eigenfunctions or modes. Because these POD coefficients and modes correspond to different flow structures with dissimilar length scales, this technique is particularly useful in isolating the behavior of coherent and incoherent flow structures associated with complex flowfields. For the sake of brevity, readers are advised to refer to Lumley [16], Aubry et al. [17], Arndt et al. [18], Kim et al. [19], and Shi et al. [20] for more details on the POD technique.

III. Results and Discussions

A. Near-Field Vortex Structures and Behavior

To shed light upon the near-field vortex structures and their behavior along the upper surfaces of the corrugated aerofoils, particle-streak visualizations and reconstructed vorticity fields taken at $\alpha = 0$, 10, 15, and 20 deg are presented in Figs. 3 and 4. To begin with, for the reference NACA 0010 aerofoil presented in Figs. 3a and 4a, no discernible flow separations can be detected along the aerofoil surface at $\alpha = 0$ deg, though mild flow separations that reattach back to the aerofoil surface can be seen to occur at $\alpha = 10$ deg. As the angle of attack increases further to $\alpha = 15$ and 20 deg, flow-separation regions become larger with regular formation of large-scale flow-separation vortices. These observations are in line with typical NACA aerofoil flow phenomena at relatively low Reynolds number (Kim et al. [21] and Kojima et al. [22]) and set a benchmark for subsequent comparisons with the corrugated aerofoils.

For corrugated A aerofoil, Figs. 3b and 4b show that small-scale flow separations occur at the sharp corrugation peaks along the upper surface at $\alpha = 0$ deg and form small recirculating vortices within the valleys. At this angle of attack, they are trapped within the valleys and thus do not convect downstream. Flows further away from the corrugations remain relatively stable and drive the recirculating vortices within the valleys. These observations are consistent with those made by Hu and Tamai [9] and Murphy and Hu [10]. As the angle of attack increases to $\alpha = 10$ and 15 deg, the flow-separation behavior becomes worse than that of the NACA 0010 aerofoil at a similar angle of attack. The separated flow regions are visually larger and more incoherent. Closer inspection of the second and third images in Fig. 3b indicates that this is due to strong flow separations occurring immediately along the blunt leading edge, which are in turn accentuated by the corrugations located downstream. Furthermore, note that the corrugations themselves led to the production of spanwise vorticity, which contributes toward the overall flow-separation behavior.

Recirculating vortices can still be observed to form within the valleys at $\alpha = 15$ deg, though they now tend to escape the confines of the valleys and merge into the flow-separation region. This signifies the increasing ineffectiveness of the corrugations to trap recirculating vortices reliably at higher angles of attack under the present test conditions. At $\alpha = 20$ deg, the flow-separation region above this aerofoil is comparable to that of the NACA 0010 aerofoil, and it continues to exhibit increased flow incoherence. One likely reason for this observation is that reversed flows at high angles of attack will see fluid being directed upstream toward the leading edge. Unlike the smooth NACA 0010 aerofoil, sharp corrugations along the upper surface of corrugated A aerofoil will lead to multiple minor flow separations and promote flow incoherence as they move upstream. Furthermore, it is also plausible that the comparatively lower Reynolds number used here means that the freestream momentum is not sufficiently strong to deter such behavior.

Compared to [9,10], where the Reynolds numbers used were much larger, the preceding observations show that the use of corrugated A aerofoil in a significantly lower-Reynolds-number freestream does not lead to any significant improvements to the flow-separation behavior, as compared to an NACA 0010 aerofoil. In fact, the flow-separation region may increase in relative size. Hence, corrugated A aerofoil is sensitive to the freestream Reynolds number, where it is more effective at higher Reynolds numbers. This behavior can be understood if one considers the fact that the size of the flow-separation region tends to increase as the Reynolds number is reduced. As the distance between the corrugations and freestream fluid increases, the ability of the former to induce the latter to move closer to the aerofoil surface will be adversely impacted, as seen in this case.

As for corrugated B aerofoil shown in Figs. 3c and 4c, the flow also separates immediately along the leading edge at $\alpha = 0$ deg. The presence of the corrugations again produces recirculating vortices within the valley as well as the saddle. Because of differences in the size of the valley and saddle, the recirculating vortex formed in the

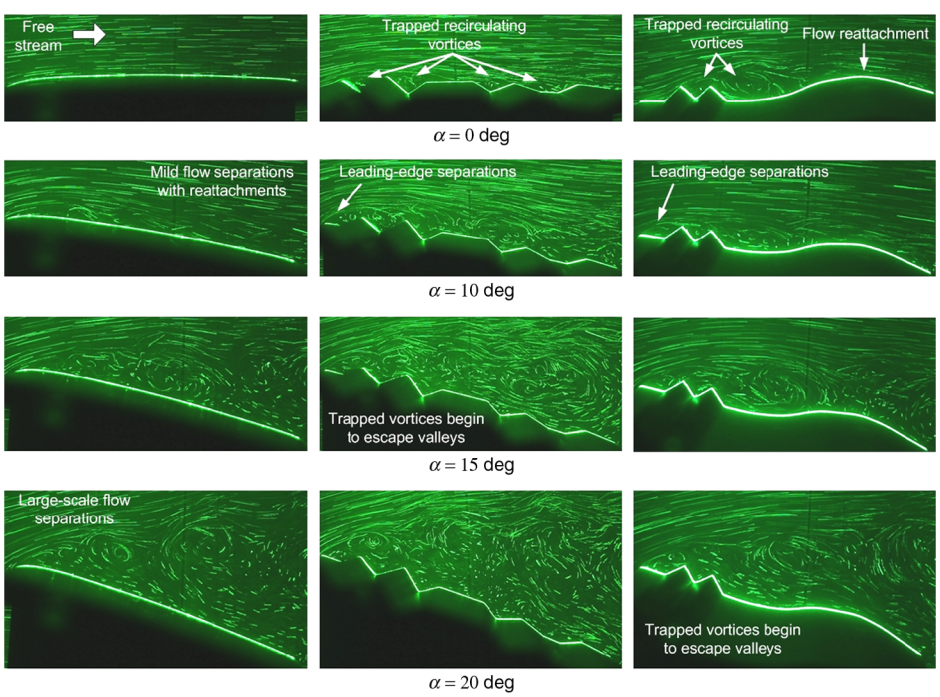

Fig. 3 Visualized instantaneous flowfields along the upper surface at $\alpha = 0$, 10, 15, and 20 deg of a) NACA 0010, b) corrugated A aerofoil, and c) corrugated B aerofoil.

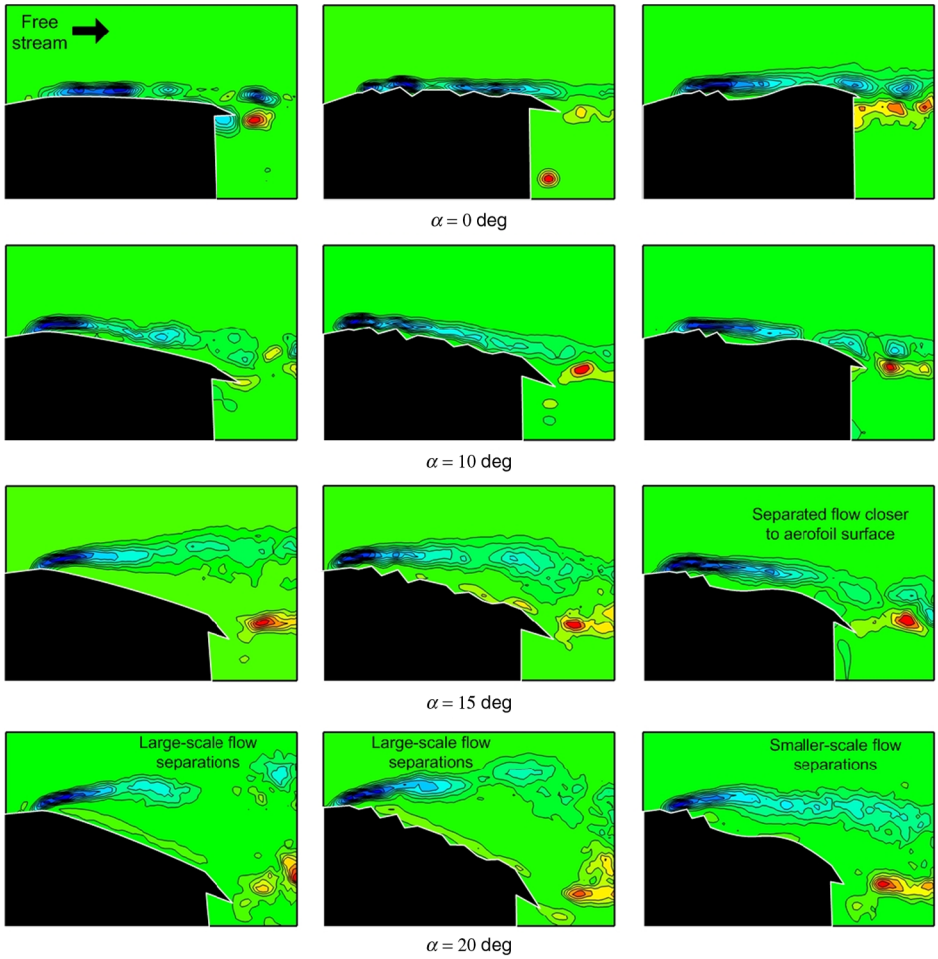

a) NACA 0010 **b) Corrugated A** **c) Corrugated B**

Fig. 4 Reconstructed instantaneous vorticity field maps at $\alpha = 0$, 10, 15, and 20 deg for a) NACA 0010, b) corrugated A aerofoil, and c) corrugated B aerofoil.

latter will be significantly larger, though its size is constrained by the presence of the trailing-edge hump. As a result, the flow reattaches to the aerofoil upper surface before leaving the aerofoil.

When the angle of attack increases to $\alpha = 10$ deg, this aerofoil continues to limit the growth of the separated flow region through the combined actions of the recirculating vortex at the saddle and trailing-edge hump. In fact, a comparison between all three aerofoils here will show that corrugated B aerofoil consistently produces the smallest flow-separation regions above the aerofoil surface at $\alpha = 10$ deg and beyond. This is despite the fact that the corrugations in corrugated B aerofoil produce spanwise vorticity in a relatively similar manner as corrugated A aerofoil. However, note that the trailing-edge hump has smaller effects in preventing the recirculating vortex from escaping the saddle at higher angles of attack. Last, it is also interesting to note that flow-separation vortices produced along the leading-edge of corrugated B aerofoil at $\alpha = 20$ deg tend to be of smaller scale, compared to both NACA 0010 and corrugated A aerofoils. Generally speaking, the near-wall flow behavior of the corrugated aerofoils here are comparable to those observed by Hu and Tamai [9], Murphy and Hu [10], and Levy and Seifert [11], even if their effects on the overall large-scale flow-separation behavior differ.

B. Flow-Separation Bubble Size

Instantaneous results presented in Figs. 3 and 4 have so far shown that corrugated B aerofoil exhibits more favorable flow-separation control behavior than corrugated A aerofoil and that the latter does not necessarily perform better than NACA 0010 aerofoil at the present working conditions. To ascertain that these observations continue to hold true in a more persistent manner, streamlines derived from mean PIV velocity fields are presented in Fig. 5 to inspect the resultant flow-separation bubbles. From the figure, recirculating regions are formed above both corrugated aerofoils, particularly for corrugated B aerofoil. In fact, the recirculating region at the saddle of corrugated B aerofoil can be observed even at $\alpha = 0$ deg, due to its relatively larger physical size. In contrast, some of the small-scale recirculating regions trapped within the valleys of both corrugated aerofoils are not captured in these streamline results, due to their unsteady nature and limited PIV measurement resolution. Nevertheless, particle-streak visualizations presented earlier have fully ascertained that they are indeed present.

As the angle of attack increases to $\alpha = 10$ deg, at least one of these recirculating regions can be observed within the corrugation valleys in the streamline results of corrugated A aerofoil. For corrugated B aerofoil, the large-scale recirculating region remains present and bounded by the trailing-edge hump. In contrast, mean streamlines of the NACA 0010 aerofoil follow the upper surface closely with no recirculating region formed, as expected. At $\alpha = 15$ deg, the corrugated aerofoils clearly demonstrate their ability in reducing flow separations, with significantly smaller flow-separation regions as compared to the NACA 0010 aerofoil, especially for corrugated B aerofoil. Closer inspection reveals that it does not produce a flow-separation bubble at all. Other than the recirculating region at the saddle, the flow remains attached to the aerofoil upper surface. This observation supports the earlier notion that the recirculating vortex plays an important role in producing this favorable behavior. Therefore, it appears that a single but physically larger recirculating region is able to exert more favorable flow influences than multiple, smaller recirculating vortices found in corrugated A aerofoil. The third image of Fig. 5b suggests that reversed flows along corrugated

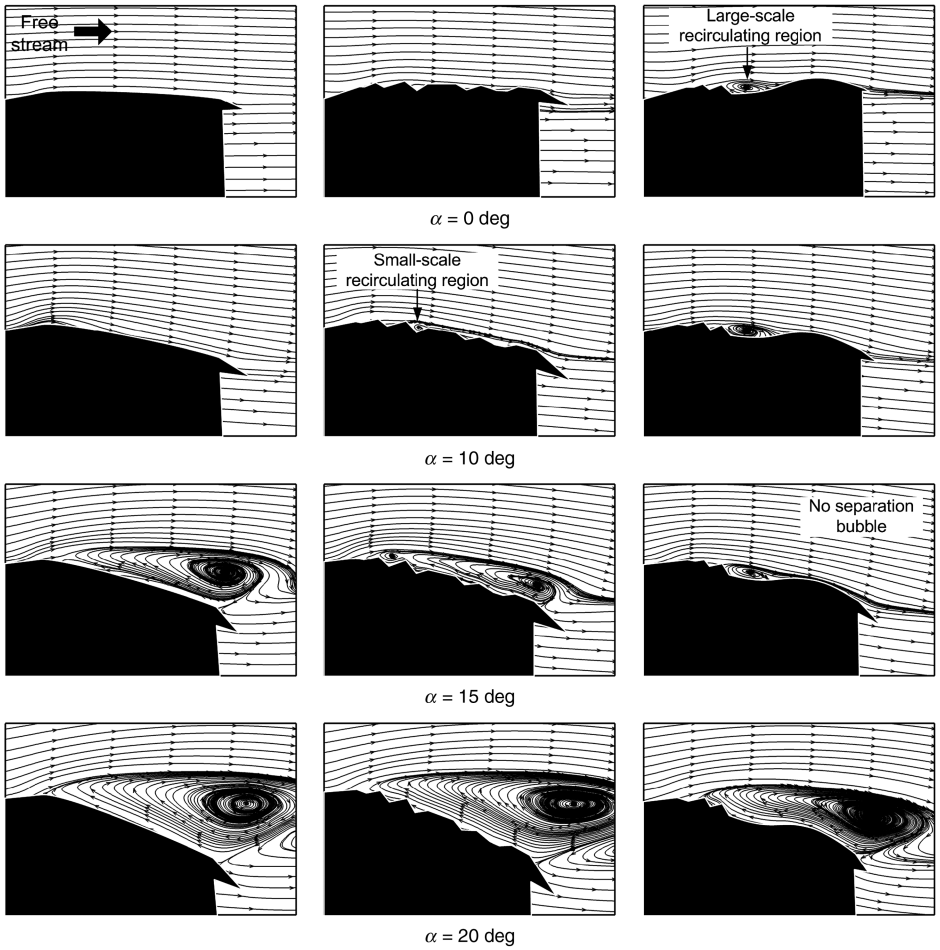

a) NACA 0010 b) Corrugated A c) Corrugated B

Fig. 5 Mean flow streamlines at $\alpha = 0$, 10, 15, and 20 deg of a) NACA 0010, b) corrugated A aerofoil, and c) corrugated B aerofoil.

A aerofoil upper surface disrupt the small-scale recirculating regions and render them less effective as the angle of attack increases.

At $\alpha = 20$ deg, however, there is no practical difference in flow-separation bubble size between NACA 0010 and corrugated A aerofoils, and corrugated B aerofoil also loses its effectiveness in reducing flow-separation bubble size. Result shows that the flow-separation region grows dramatically along the corrugated B aerofoil leading edge, and its recirculating region does not exert significant favorable flow effects, though it still manages to produce the smallest flow-separation bubble at this point. Through these preceding comparisons, it is clear that corrugated B aerofoil is able to limit the size of the flow-separation bubble most effectively out of all three test aerofoils up to $\alpha = 20$ deg, which supports the vortical behavior presented earlier. Note that Hu and Tamai [9] had earlier shown that the lift coefficient for their corrugated aerofoil was higher than that of an NACA aerofoil when the corrugated aerofoil produced comparatively smaller flow-separation bubbles. Therefore, it is expected that the smaller flow-separation bubbles observed in corrugated B aerofoil here will lead to similar aerodynamic behavior.

IV. Conclusions

Present results show that, at $Re = 14,000$, small recirculating vortices within the valleys of corrugated A aerofoil do not draw freestream fluid closer to the aerofoil upper surface as well as those observed at significantly higher Reynolds numbers. Therefore, its flow-separation bubble sizes are comparable to those for NACA 0010 aerofoil. In contrast, corrugated B aerofoil demonstrates better flow-separation control behavior and, as a result, produces significantly smaller flow-separation bubbles than corrugated A and NACA 0010 aerofoils. This can be attributed to the formation of a relatively large-scale recirculating region at its saddle location. Results indicate that this physically larger recirculating region works better than multiple small recirculating regions in mitigating flow-separation behavior. Additionally, the trailing-edge hump also enables flow reattachment, which reduces flow-separation bubble size. Although the favorable effects by corrugated B aerofoil geometry diminish as the angle of attack increases, it consistently produces the best flow-separation control characteristics among the currently studied aerofoils and test conditions here.

Acknowledgments

The authors wish to acknowledge the support of the study by the MINDEF-NTU-JPP/10/09 grant, the Undergraduate Research Experience on Campus program of Nanyang Technological University, and the Advanced Research Programme of the National University of Singapore High School of Maths and Science.

References

[1] Freymuth, P., "Thrust Generation by an Airfoil in Hover Modes," *Experiments in Fluids*, Vol. 9, Nos. 1–2, 1990, pp. 17–24. doi:10.1007/BF00575331

[2] Triantafyllou, M. S., Triantafyllou, G. S., and Gopalkrishnan, R., "Wake Mechanics for Thrust Generation in Oscillating Foils," *Physics of Fluids*, Vol. 3, No. 12, 1991, pp. 2835–2837. doi:10.1063/1.858173

[3] Dickinson, M. H., Lehmann, F.-O., and Sane, S. P., "Wing Rotation and the Aerodynamic Basis of Insect Flight," *Science*, Vol. 284, No. 5422, 1999, pp. 1954–1960. doi:10.1126/science.284.5422.1954

[4] Ellington, C. P., "The Novel Aerodynamics of Insect Flight: Applications to MicroAir Vehicles," *Journal of Experimental Biology*, Vol. 202, No. 23, 1999, pp. 3439–3448. doi:10.1016/S0065-2806(08)60094-6

[5] Lai, J. C. S., and Platzer, M. F., "Jet Characteristics of a Plunging Airfoil," *AIAA Journal*, Vol. 37, No. 12, 1999, pp. 1529–1537. doi:10.2514/3.14353

[6] Wang, Z. J., "Vortex Shedding and Frequency Selection in Flapping Flight," *Journal of Fluid Mechanics*, Vol. 410, 2000, pp. 323–341. doi:10.1017/S0022112099008071

[7] Sane, S. P., "The Aerodynamics of Insect Flight," *Journal of Experimental Biology*, Vol. 206, No. 23, 2003, pp. 4191–4208. doi:10.1242/jeb.00663

[8] Lua, K. B., Lim, T. T., and Yeo, K. S., "Aerodynamic Forces and Flow Fields of a Two-Dimensional Hovering Wing," *Experiments in Fluids*, Vol. 45, No. 6, 2008, pp. 1047–1065. doi:10.1007/s00348-008-0527-z

[9] Hu, H., and Tamai, M., "Bioinspired Corrugated Airfoil at Low Reynolds Numbers," *Journal of Aircraft*, Vol. 45, No. 6, 2008, pp. 2068–2077. doi:10.2514/1.37173

[10] Murphy, J. T., and Hu, H., "An Experimental Study of a Bio-Inspired Corrugated Airfoil for Micro Air Vehicle Applications," *Experiments in Fluids*, Vol. 49, No. 2, 2010, pp. 531–546. doi:10.1007/s00348-010-0826-z

[11] Levy, D.-E., and Seifert, A., "Simplified Dragonfly Airfoil Aerodynamics at Reynolds Numbers Below 8000," *Physics of Fluids*, Vol. 21, No. 7, 2009, p. 071901. doi:10.1063/1.3166867

[12] Keane, R. D., and Adrian, R. J., "Theory of Cross-Correlation Analysis of PIV Images," *Applied Scientific Research*, Vol. 49, No. 3, 1992, pp. 191–215. doi:10.1007/BF00384623

[13] Sirovich, L., "Turbulence and the Dynamics of Coherent Structures, I-Coherent Structures, II-Symmetries and Transformations, III-Dynamics and Scaling," *Quarterly of Applied Mathematics*, Vol. 45, 1987, pp. 561–590.

[14] Berkooz, G., Holmes, P., and Lumley, J. L., "The Proper Orthogonal Decomposition in the Analysis of Turbulent Flows," *Annual Review in Fluid Mechanics*, Vol. 25, 1993, pp. 539–575. doi:10.1146/annurev.fluid.25.1.539

[15] Chatterjee, A., "An Introduction to the Proper Orthogonal Decomposition," *Current Science*, Vol. 78, 2000, pp. 808–817.

[16] Lumley, J. L., "The Structure of Inhomogeneous Turbulent Flows," *Atmospheric Turbulence and Radio Wave Propagation*, edited by Yaglom, A. M., and Tatarski, V. I., Navko, Moscow, 1967, pp. 166–178.

[17] Aubry, N., Holmes, P., Lumley, J. L., and Stone, E., "The Dynamics of Coherent Structures in the Wall Region of a Turbulent Boundary Layer," *Journal of Fluid Mechanics*, Vol. 192, 1988, pp. 115–173. doi:10.1017/S0022112088001818

[18] Arndt, R. E., Long, D. F., and Glauser, M. N., "The Proper Orthogonal Decomposition of Pressure Fluctuations Surrounding a Turbulent Jet," *Journal of Fluid Mechanics*, Vol. 340, 1997, pp. 1–33. doi:10.1017/S0022112097005089

[19] Kim, Y., Rockwell, D., and Liakopoulos, A., "Vortex Buffeting of Aircraft Tail: Interpretation via Proper Orthogonal Decomposition," *AIAA Journal*, Vol. 43, No. 3, 2005, pp. 550–559. doi:10.2514/1.9989

[20] Shi, S., New, T. H., and Liu, Y., "Flapping Dynamics of a Low Aspect-Ratio Energy-Harvesting Membrane Immersed in a Square Cylinder Wake," *Experimental Thermal and Fluid Science*, Vol. 46, 2013, pp. 151–161. doi:10.1016/j.expthermflusci.2012.12.007

[21] Kim, D.-H., Chang, J.-W., and Chung, J., "Low-Reynolds-Number Effect on Aerodynamic Characteristics of a NACA 0012 Airfoil," *Journal of Aircraft*, Vol. 48, No. 4, 2011, pp. 1212–1215. doi:10.2514/1.C031223

[22] Kojima, R., Nonomura, T., Oyama, A., and Fujii, K., "Large-Eddy Simulation of Low-Reynolds-Number Flow over Thick and Thin NACA Airfoils," *Journal of Aircraft*, Vol. 50, No. 1, 2013, pp. 187–196. doi:10.2514/1.C031849

L. Cattafesta
Associate Editor